ADVANCED FUNCTIONAL MATERIALS
www.afm-journal.de

Hydroxylated Ionic Liquids as Functional Additives for Stable Aqueous Zn Batteries

Qiang Yan, Yucheng Liu, Wenxu Zhu, Shengjun Xu, Ho Mei Law, Jingwei Li, and Francesco Ciucci**

Rechargeable zinc (Zn) metal batteries are promising for large-scale energy storage due to their safety and affordability. However, Zn anodes in aqueous electrolytes suffer from uneven deposition and side reactions that impair battery performance and shorten lifespan. Herein, the use of a hydroxyl-functionalized ionic liquid, 1-hydroxyethyl-3-methylimidazolium triflate (HO-EMImTfO), as an electrolyte additive to stabilize the Zn anode is reported for the first time. This hydroxyl-functionalized ionic liquid acts through a dual mechanism: 1) the hydroxyl (—OH) group of HO-EMIm$^+$ integrates into the Zn^{2+} solvation shell by displacing water molecules, altering the solvation structure, and suppressing water-induced side reactions; 2) HO-EMIm$^+$ accumulates on the Zn surface, forming a HO-EMIm$^+$-rich layer that facilitates lateral Zn^{2+} diffusion, promoting a uniform Zn deposition. The modulation of the Zn^{2+} solvation environment and interfacial ion flux effectively suppresses Zn pulverization and dendrite formation. Consequently, Zn||Cu cells with HO-EMImTfO achieve an average Coulombic efficiency of 99.5% over 1000 cycles at 4 mA cm^{-2}, and Zn||V_2O_5 full cells retain 223.5 mAh g^{-1} after 1265 cycles at 1 A g^{-1}. This work demonstrates the potential of strategically designed hydroxyl-functionalized ionic liquids for durable aqueous Zn batteries.

1. Introduction

Rechargeable zinc (Zn) metal batteries have emerged as a promising solution for large-scale energy storage, owing to their inherent safety, environmental friendliness, and low cost.[1,2] However, the practical deployment of Zn technology is hindered by several challenges associated with the Zn anode, particularly in aqueous electrolytes. These challenges include dendrite formation, surface corrosion, Zn pulverization, and parasitic hydrogen evolution,[3–5] which lead to poor cycling stability, low Coulombic efficiency, and potential safety hazards. To address these issues, various strategies have been explored, including protective surface coatings,[6,7] separator modifications,[8,9] and electrolyte formulation adjustments.[10–14] Among these approaches, tailoring the electrolyte with functional additives is particularly attractive due to its simplicity, minimal impact on energy density, and its scalability.[15] A well-chosen functional additive can directly regulate interfacial chemistry and Zn^{2+} deposition behavior in situ, thus addressing the root causes of anode instability without complex cell redesign.

One effective class of electrolyte additives for aqueous Zn batteries comprises small molecules containing hydroxyl (—OH) groups (e.g., methanol[16,17] and ethylene glycol[18,19]). These —OH-containing additives stabilize Zn plating/stripping by partially replacing H_2O molecules in the Zn^{2+} solvation sheath.[20] By coordinating with Zn^{2+}, —OH groups reduce the amount of free water at the electrode interface, thereby lowering water activity and mitigating its involvement in undesirable side reactions.[21–23] Nevertheless, while small organic and —OH-containing additives can effectively modulate Zn^{2+} solvation and interfacial chemistry, they often have high volatility or limited ability to influence the spatial distribution of Zn^{2+} ions during deposition.

Recent studies have revealed that Zn pulverization, the gradual crumbling of Zn metal due to repeated Zn plating and stripping, is an equally critical failure mode alongside the creation of dendrites.[24] To address Zn pulverization, researchers have turned to ionic liquid (IL) additives, particularly imidazolium cations. Recently, Wang et al. introduced 1-ethyl-3-methylimidazolium (EMIm$^+$) into a Zn electrolyte to create

Q. Yan, Y. Liu, W. Zhu
College of Chemistry
Liaoning University
Shenyang 110036, P. R. China
Q. Yan
Institute of Dispersed Element Chemistry
Liaoning University
Shenyang 110036, P. R. China
S. Xu, H. M. Law, J. Li, F. Ciucci
Chair of Electrode Design for Electrochemical Energy Systems
University of Bayreuth
95448 Bayreuth, Bavaria, Germany
E-mail: shengjun.xu@uni-bayreuth.de; francesco.ciucci@uni-bayreuth.de
S. Xu, H. M. Law, J. Li, F. Ciucci
Bavarian Center for Battery Technology (BayBatt)
95447 Bayreuth, Bavaria, Germany

The ORCID identification number(s) for the author(s) of this article can be found under https://doi.org/10.1002/adfm.202512706

DOI: 10.1002/adfm.202512706

an "ion-diversion dam" at the Zn/electrolyte interface.[24] Adsorbed $EMIm^+$ cations form a cation-rich layer on the Zn surface that redistributes incoming Zn^{2+} laterally, hindering direct Zn^{2+} flux perpendicular to the Zn surface.[25] The forced lateral diffusion prevents localized Zn^{2+} build-up, effectively suppressing Zn pulverization. Imidazolium IL additives such as $EMIm^+$, [26,27] methylimidazolium (MIM^+),[28] and 1-butyl-3-methylimidazolium (BMI^+)[29,30] have therefore become effective stabilizers for Zn anodes due to this potential "ion-diversion" effect, along with their non-volatile characteristics and adaptable chemical structures.[31–33] While conventional imidazolium-based ILs can favorably influence ion flux at the interface, their typical lack of polar functional groups means they do not significantly modify the Zn^{2+} solvation structure. This oversight leaves water-induced issues, such as corrosion and hydrogen evolution, largely unaddressed. Conversely, while small hydroxyl-containing molecules can alter solvation, they often lack the interfacial flux control and stability of ILs. This highlights a critical need for additives that concurrently manage both Zn^{2+} solvation and interfacial dynamics. While individual components of this strategy (hydroxylation or ILs) have been explored, their synergistic integration within a single hydroxyl-functionalized ionic liquid to achieve simultaneous solvation control and interfacial flux regulation for aqueous Zn anodes has remained unexplored.

Motivated by the complementary advantages of hydroxyl groups for Zn^{2+} solvation control and imidazolium cations for interfacial ion-flux regulation, here we introduce a hydroxyl-functionalized imidazolium additive as a dual-function electrolyte modifier for aqueous Zn batteries. In particular, we employ the 1-hydroxyethyl-3-methylimidazolium cation ($HO\text{-}EMIm^+$, see chemical structure in **Figure 1a**) paired with triflate anions (TfO^-) as an additive in the $Zn(TfO)_2$ electrolyte. During Zn electrodeposition, the $HO\text{-}EMIm^+$ cations concentrate near the Zn anode surface, assembling into a dense cation-enriched interfacial layer. This $HO\text{-}EMIm^+$-rich layer serves as an ion-diversion dam that redistributes Zn^{2+} flux laterally across the electrode and, in turn, alleviates Zn oversaturation and pulverization. Simultaneously, the —OH group of $HO\text{-}EMIm^+$ partially replaces H_2O in the Zn^{2+} solvation sheath, reducing interfacial free-water activity and suppressing water-induced side reactions. Owing to this synergistic dual action on interfacial chemistry, Zn||Cu cells with the $HO\text{-}EMIm^+$ additive exhibit enhanced Zn plating/stripping reversibility, achieving an average Coulombic efficiency of 99.5% over 1000 cycles at a current density of 4 mA cm^{-2}. Full Zn||V_2O_5 batteries also demonstrate improved longevity, sustaining stable cycling for over 1200 cycles at 1 A g^{-1} (even up to 4000 cycles at 2 A g^{-1} with more than 53% capacity retention). These results underscore the effectiveness of the HO-EMImTfO additive in mitigating Zn pulverization issues and water-induced side reactions.

2. Results and Discussion

2.1. Modulating Interfacial Interactions

To elucidate the molecular-level interactions between ionic liquids and Zn metal anodes, the adsorption energies of Zn^{2+}, $EMIm^+$, and $HO\text{-}EMIm^+$ cations on a Zn surface were calculated. As shown in Figure 1b, $HO\text{-}EMIm^+$ exhibits the most negative adsorption energy (−2.36 eV), indicating the strongest affinity toward the Zn surface among the three species. This strong preferential adsorption of $HO\text{-}EMIm^+$ is crucial for establishing a robust $HO\text{-}EMIm^+$-rich layer at the Zn/electrolyte interface, which is hypothesized to act as the "ion-diversion dam."[34,35] To further investigate the influence of ionic liquid additives on Zn^{2+} solvation, molecular dynamics (MD) simulations were performed (Figure S1, Supporting Information). In all electrolytes, pronounced Zn—O_TfO^- and Zn—O_H_2O peaks were observed (Figure 1c–e), confirming the presence of a primary hydration shell around Zn^{2+}. However, in the electrolyte containing $EMIm^+$, no $EMIm^+$ appears in the first solvation shell of Zn^{2+} (Figure 1d), suggesting that $EMIm^+$ does not coordinate with Zn^{2+}. In contrast, when $HO\text{-}EMIm^+$ is present, a distinct $HO\text{-}EMIm^+$ signal emerges in the first solvation shell of Zn^{2+} (Figure 1e), indicating direct involvement of $HO\text{-}EMIm^+$ in Zn^{2+} solvation. Coordination number (CN) analysis further quantified these solvation changes: in the baseline electrolyte, Zn^{2+} is coordinated by approximately five water molecules (CN = 5.09, Figure 1c), whereas adding $EMIm^+$ only slightly lowers this CN to 5.01 (Figure 1d), indicating minimal disruption of Zn^{2+} hydration. In contrast, including $HO\text{-}EMIm^+$ reduces the CN significantly to 4.90 (Figure 1e), demonstrating that $HO\text{-}EMIm^+$ disrupts the Zn^{2+} hydration shell by partially replacing water molecules.[36] This altered solvation environment is expected to suppress water-induced side reactions such as hydrogen evolution and corrosion, thereby enhancing interfacial stability.[37,38] DFT calculations were conducted to investigate the desolvation behavior of Zn^{2+} in relation to two proposed complexes derived from MD simulation results (Figure S2, Supporting Information). In the $Zn^{2+}{\cdot}5(H_2O){\cdot}TfO^-$ model, removing a water molecule requires only 0.72 eV, compared to 8.55 eV needed to remove TfO^-. Similarly, in $Zn^{2+}{\cdot}5(H_2O){\cdot}HO\text{-}EMIm^+$, the $HO\text{-}EMIm^+$ cation binds more strongly to Zn^{2+} (2.42 eV) than a water molecule does (1.23 eV). These results suggest a comparable stepwise desolvation behavior in both cases, where water is removed before the TfO^- or $HO\text{-}EMIm^+$. This desolvation pathway was further analyzed for the HO-EMImTfO electrolyte (Figure S3, Supporting Information).

To illustrate the interfacial challenges of Zn metal anodes in aqueous electrolytes, we first examined a model system comprising a plain $Zn(TfO)_2$ solution without additives.[39] As depicted in Figure 1f (left), Zn^{2+} ions are surrounded by a fully hydrated shell. This environment facilitates parasitic reactions such as hydrogen evolution and corrosion, which in turn accelerate electrolyte consumption, Zn pulverization, and dendrite formation.[40] Based on the above theoretical calculation results, we introduced $HO\text{-}EMIm^+$ as an electrolyte additive to construct a functional "ion-diversion dam" at the Zn/electrolyte interface (Figure 1f, right). The —OH groups in $HO\text{-}EMIm^+$ play a critical role in modulating the Zn^{2+} solvation structure. Replacing coordinated water molecules and interacting with free water reduces the number of active water molecules near the Zn electrode, further suppressing water-related parasitic reactions.[36–38] Owing to their strongest adsorption energy (Figure 1b), $HO\text{-}EMIm^+$ cations accumulate on the Zn surface, resulting in a more compact $HO\text{-}EMIm^+$-rich interfacial layer compared to $EMIm^+$ (Figure 1f). To verify the formation of a $HO\text{-}EMIm^+$-rich interfacial layer, we simulated the charging process under a

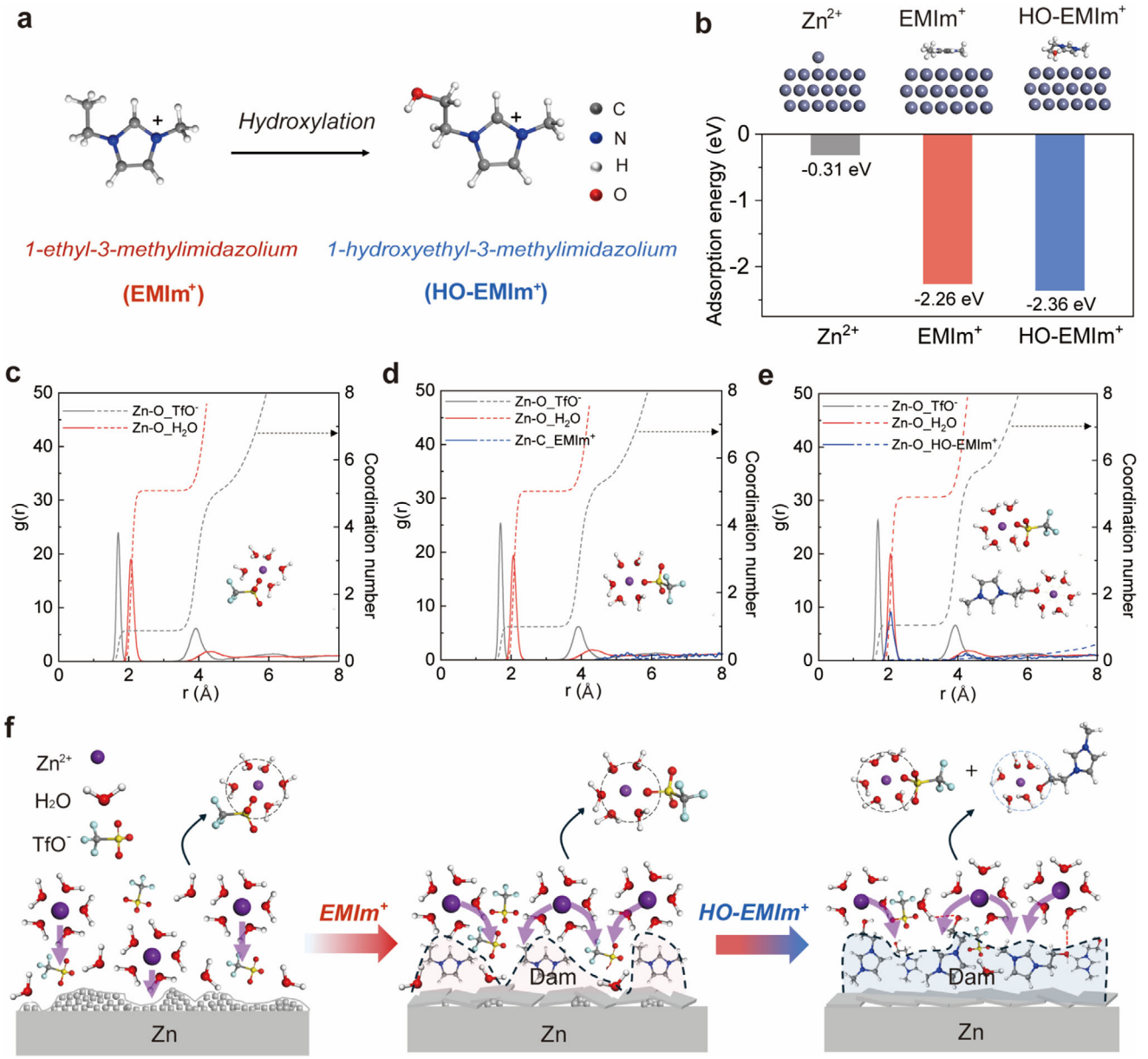

Figure 1. Interfacial design and solvation modulation by HO-EMIm$^+$. a) Chemical structures of two ionic liquid cations (EMIm$^+$ and HO-EMIm$^+$). b) Calculated Zn^{2+}, EMIm$^+$, and HO-EMIm$^+$ adsorption energies on a Zn metal surface. Radial distribution functions (RDFs) from MD simulations of c) 2 M $Zn(TfO)_2$, d) 2 M $Zn(TfO)_2$ with EMImTfO additive, and e) 2 M $Zn(TfO)_2$ with HO-EMImTfO additives. f) Schematic illustration of Zn^{2+} solvation sheaths and Zn anode interfaces without additives (left) and with EMIm$^+$ (middle) and HO-EMIm$^+$ (right). The additive-free interface enables direct Zn^{2+} plating, resulting in dendrites and pulverization, whereas the EMIm$^+$/HO-EMIm$^+$ additive creates a cationic "ion-diversion dam" that redirects Zn^{2+} flux laterally for uniform deposition.

constant electric field. The simulation (Figure S4a, Supporting Information) shows that HO-EMIm$^+$ cations gradually assemble into a compact interfacial layer due to electric-field-driven attraction to the Zn surface. The mass density profile (Figure S4b, Supporting Information) reveals that this layer extends ≈30 Å from the surface. Furthermore, calculated Zn^{2+} diffusion coefficients (Figure S4c,d, Supporting Information) indicate that cross-plane Zn^{2+} diffusion (across the HO-EMIm$^+$-rich interfacial layer) is significantly suppressed, whereas in-plane diffusion (parallel to the Zn electrode surface) remains active. As a result, the HO-EMIm$^+$-rich layer impedes direct Zn^{2+} transport toward the Zn electrode and instead promotes lateral ion movement, leading to more uniform Zn deposition.

2.2. Interfacial Stabilization

To assess the interfacial stability imparted by the ionic liquid additive, Zn||Zn symmetric cells were assembled and subjected to long-term galvanostatic cycling tests using electrolytes with

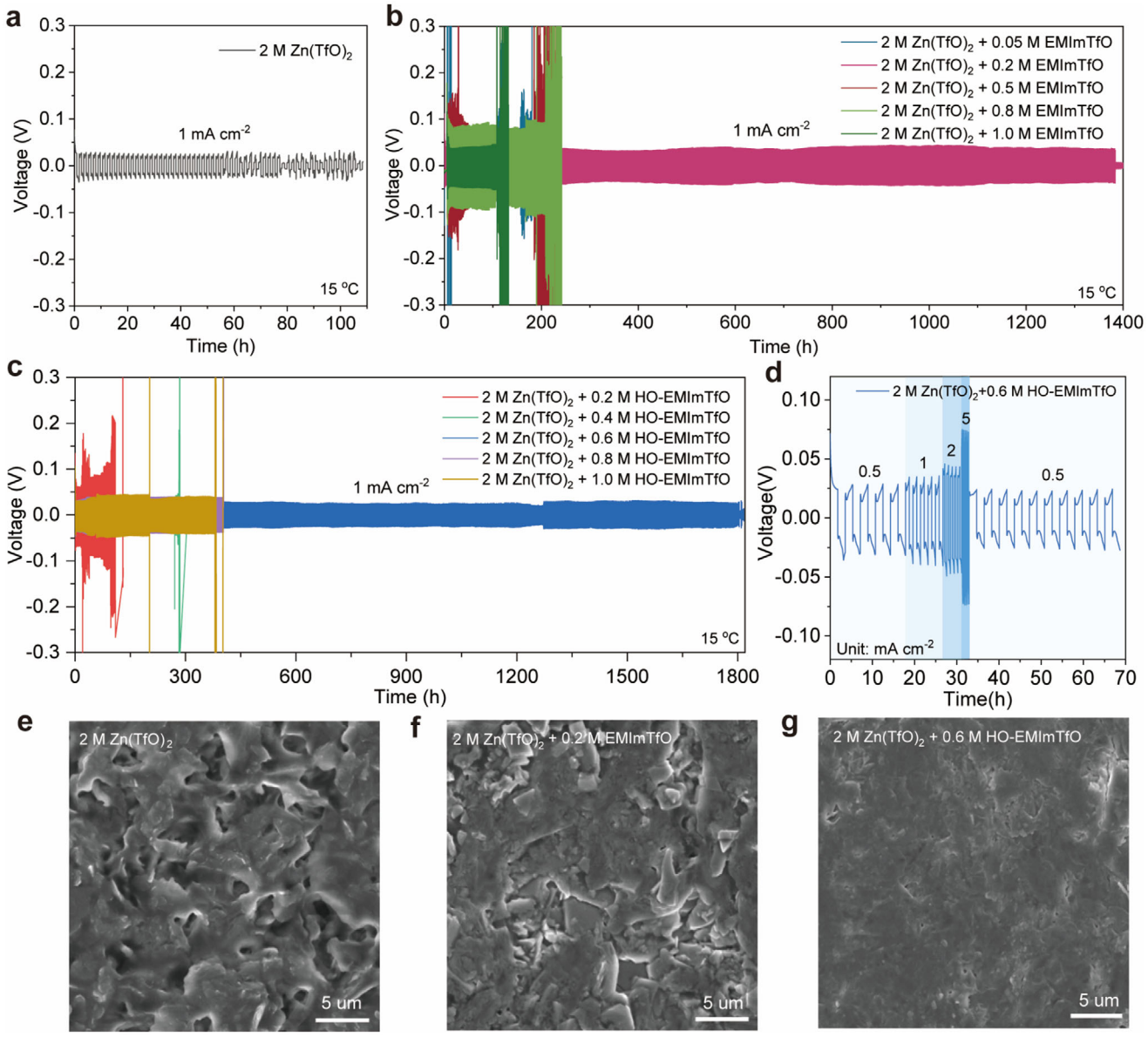

Figure 2. Electrochemical stability and corrosion suppression. a) Cycling performance of symmetric Zn||Zn cells utilizing a 2 м $Zn(TfO)_2$ electrolyte. b) Cycling performance of symmetric Zn||Zn cells using electrolytes with varying concentrations of EMImTfO additives. c) Cycling performance of symmetric Zn||Zn cells employing electrolytes with varying concentrations of HO-EMImTfO additives. d) Rate performance of Zn||Zn symmetric cells in 2 м $Zn(TfO)_2$ + 0.6 м HO-EMImTfO electrolyte. SEM images of Zn metal after 7 days immersion in e) 2 м $Zn(TfO)_2$, f) 2 м $Zn(TfO)_2$ + 0.2 м EMImTfO, and g) 2 м $Zn(TfO)_2$ + 0.6 м HO-EMImTfO electrolytes.

various additive concentrations. At a current density of 1 mA cm^{-2}, the Zn||Zn symmetric cell with the additive-free baseline electrolyte exhibited a limited cycling lifespan of ≈60 h (**Figure 2a**), whereas the cell containing 0.2 м EMImTfO showed a dramatically prolonged lifespan of 1380 h (Figure 2b; Figure S5, Supporting Information). Notably, the optimal concentration for the HO-EMImTfO additive (0.6 м) was found to be higher than that for EMImTfO (0.2 м), as depicted in Figure 2c. This difference is likely attributed to the partial partitioning of HO-$EMIm^+$ cations between the interface (where they contribute to a protective layer) and the Zn^{2+} solvation sheath, thus requiring a greater total amount to effectively saturate both roles. Accordingly, the electrolyte containing 0.6 м HO-EMImTfO enabled the symmetric cell to cycle for 1800 h before failure (Figure 2c; Figure S6, Supporting Information). The rate performance of Zn||Zn symmetric cells was evaluated over a current density range of 0.5–5.0 mA cm^{-2} (Figure 2d). When the current density was increased to 5.0 mA cm^{-2}, an overpotential of 74 mV was observed. Subsequently, upon reducing the current density back to 0.5 mA cm^{-2}, the overpotential remained stable at 23 mV, demonstrating the excellent rate response capability and compatibility of the HO-EMImTfO electrolyte. These findings underscore the significant stabilizing effect of the hydroxyl-functionalized ionic liquid additive on Zn anode performance.

To further assess interface compatibility, Zn foils were immersed for 7 days in the three electrolytes: 2 M $Zn(TfO)_2$, 2 M $Zn(TfO)_2$ with 0.2 M EMImTfO, and 2 M $Zn(TfO)_2$ with 0.6 M HO-EMImTfO. Subsequently, surface characterization was carried out using scanning electron microscopy (SEM).[41] As shown in Figure 2e–g, the Zn surfaces exhibited markedly different morphologies depending on the electrolyte. In the baseline electrolyte, the Zn foil exhibited severe surface degradation, characterized by a high porosity indicative of corrosion (Figure 2e; Figure S7, Supporting Information). Conversely, the Zn foil in 0.2 M EMImTfO showed a smoother and denser morphology (Figure 2f; Figure S8, Supporting Information), indicating that adding EMImTfO partially inhibited corrosion processes. Remarkably, the Zn surface immersed in 0.6 M HO-EMImTfO electrolyte displayed a uniform, densely packed morphology with minimal evidence of corrosion (Figure 2g; Figure S9, Supporting Information). These morphological observations are consistent with theoretical predictions that HO-EMImTfO additives mitigate water-induced corrosion.

2.3. Enhanced Zn deposition kinetics and reversibility

Electrochemical impedance spectroscopy (EIS) measurements were performed at various temperatures to elucidate the influence of ionic liquid additives on the interfacial Zn^{2+} transport and deposition kinetics (Figure S10, Supporting Information). From the EIS data, the charge transfer resistance (R_{ct}) for Zn plating/stripping was extracted. The incorporation of ionic liquid additives led to a significant decrease in R_{ct} compared to the baseline electrolyte, indicative of facilitated interfacial charge transfer (Figure S11, Supporting Information). The activation energy (E_a) for the interfacial Zn^{2+} transport and deposition reaction was then calculated by fitting R_{ct} values as a function of temperature using the Arrhenius equation.[42,43] As presented in **Figure 3a**, the baseline 2 M $Zn(TfO)_2$ electrolyte possessed the lowest E_a at 37.7 kJ mol^{-1}. In contrast, the addition of 0.2 M $EMIm^+$ increased E_a to 54.9 kJ mol^{-1}, and 0.6 M HO-$EMIm^+$ resulted in a comparable E_a of 54.3 kJ mol^{-1}. This observed increase in E_a following the introduction of $EMIm^+$ or HO-$EMIm^+$ suggests a modification of the Zn^{2+} kinetics at the Zn/electrolyte interface by the additive. Chronoamperometry (CA) at an overpotential of −150 mV provided a further examination of the dynamic Zn growth process (Figure 3b). For the baseline electrolyte, a continuous increase in deposition current from −2.98 to −27.4 mA was recorded within the initial 50 s. This phenomenon indicates an expanding electroactive surface area, likely due to dendritic growth or pulverization,[37] and this behavior aligns with the development of a porous and pulverized Zn deposit in the baseline electrolyte as subsequently confirmed by SEM analysis (Figure S12, Supporting Information). Conversely, when 0.2 M EMImTfO was added, the current exhibited a more modest rise from −2.54 to −4.44 mA over 50 s, pointing to substantially more controlled nucleation and growth (Figure S13, Supporting Information). Significantly, the electrolyte containing HO-EMImTfO maintained a stabilized deposition current at a relatively low magnitude, increasing merely from −0.83 to −2.70 mA in 50 s. Such behavior signifies the establishment of uniform nucleation sites and a homogeneous Zn^{2+} flux during plating.[44] This controlled deposition consequently fosters a more uniform current distribution, leading to dense and compact Zn deposition (Figure S14, Supporting Information).

An additional understanding of the initial nucleation behavior was gained through cyclic voltammetry (CV) measurements focusing on Zn^{2+} plating/stripping on Cu substrates (Figure 3c). The electrolyte with HO-EMImTfO demonstrated a higher nucleation overpotential (AA′′ = 11.7 mV) relative to the EMImTfO system (AA′ = 5.4 mV). This suggests a more substantial energy barrier for initial nucleation, a condition conducive to more controlled and stable Zn nucleus formation.[45,46] Consequently, the Zn deposits formed in the HO-EMImTfO electrolyte are characterized by finer grains and improved orientation, culminating in more uniform and stable growth during subsequent deposition phases. The Zn deposits were subsequently analyzed using X-ray diffraction (XRD). As shown in Figure 3d, the electrolyte composition strongly influenced the relative intensity ratio of the Zn (002) to (100) diffraction peaks. The HO-EMImTfO-containing electrolyte produced a high I(002)/I(100) ratio of 2.29, compared to 1.02 for the baseline and 0.87 for the EMImTfO-containing electrolyte. This preferential orientation along the (002) plane is highly desirable as it is recognized to facilitate more reversible Zn plating/stripping and suppress dendrite formation.[47,48] Notably, in the baseline electrolyte, additional XRD peaks corresponding to corrosion-induced byproducts were observed. High-resolution X-ray photoelectron spectroscopy (XPS) analysis was performed on Zn anodes to identify corrosion-induced byproducts. After the depth etching, XPS spectra were collected for the C 1s (Figure S15, Supporting Information), Zn 2p (Figure S16, Supporting Information), O 1s (Figure S17, Supporting Information), S 2p (Figure S18, Supporting Information), F 1s (Figure S19, Supporting Information), and N 1s (Figure S20, Supporting Information) regions. In the HO-EMImTfO system, signals corresponding to sulfate/sulfonate species (e.g., C—S, C—SO_x) and Zn—O compounds were markedly diminished, indicating that anion decomposition and water-induced corrosion were suppressed. Notably, the N 1s signal was absent, suggesting that HO-$EMIm^+$ remains electrochemically stable at the interface.

Linear sweep voltammetry (LSV) was conducted to evaluate the hydrogen evolution reaction (HER) at the Zn anode (Figure 3e). In the baseline electrolyte, the HER onset potential (at −20 mA cm^{-2}) was ≈−1.12 V. With 0.2 M EMImTfO, the HER onset shifted negatively to ≈−1.21 V, and with 0.6 M HO-EMImTfO it further shifted to −1.36 V. This progressively more negative onset indicates that hydrogen evolution was effectively suppressed by HO-EMImTfO, thereby contributing to enhanced interfacial stability. Corroborating these findings, Tafel plots were conducted to evaluate the anti-corrosion performance (Figure 3f). The HO-EMImTfO-containing electrolyte exhibits a reduced exchange current density (0.23 mA cm^{-2}), substantially lower than those in the EMImTfO (0.43 mA cm^{-2}) and baseline (2.74 mA cm^{-2}) electrolytes, further confirming the superior corrosion protection provided by the HO-EMImTfO additive.[49,50] Additionally, the wettability of the electrolytes on Zn metal was evaluated by contact angle measurements (Figure S21, Supporting Information). The HO-EMImTfO-containing electrolyte exhibited a smaller contact angle (56.7°) than the baseline electrolyte (76.7°), indicating better interfacial affinity.[51] To further examine the influence of the HO-EMImTfO additive on Zn

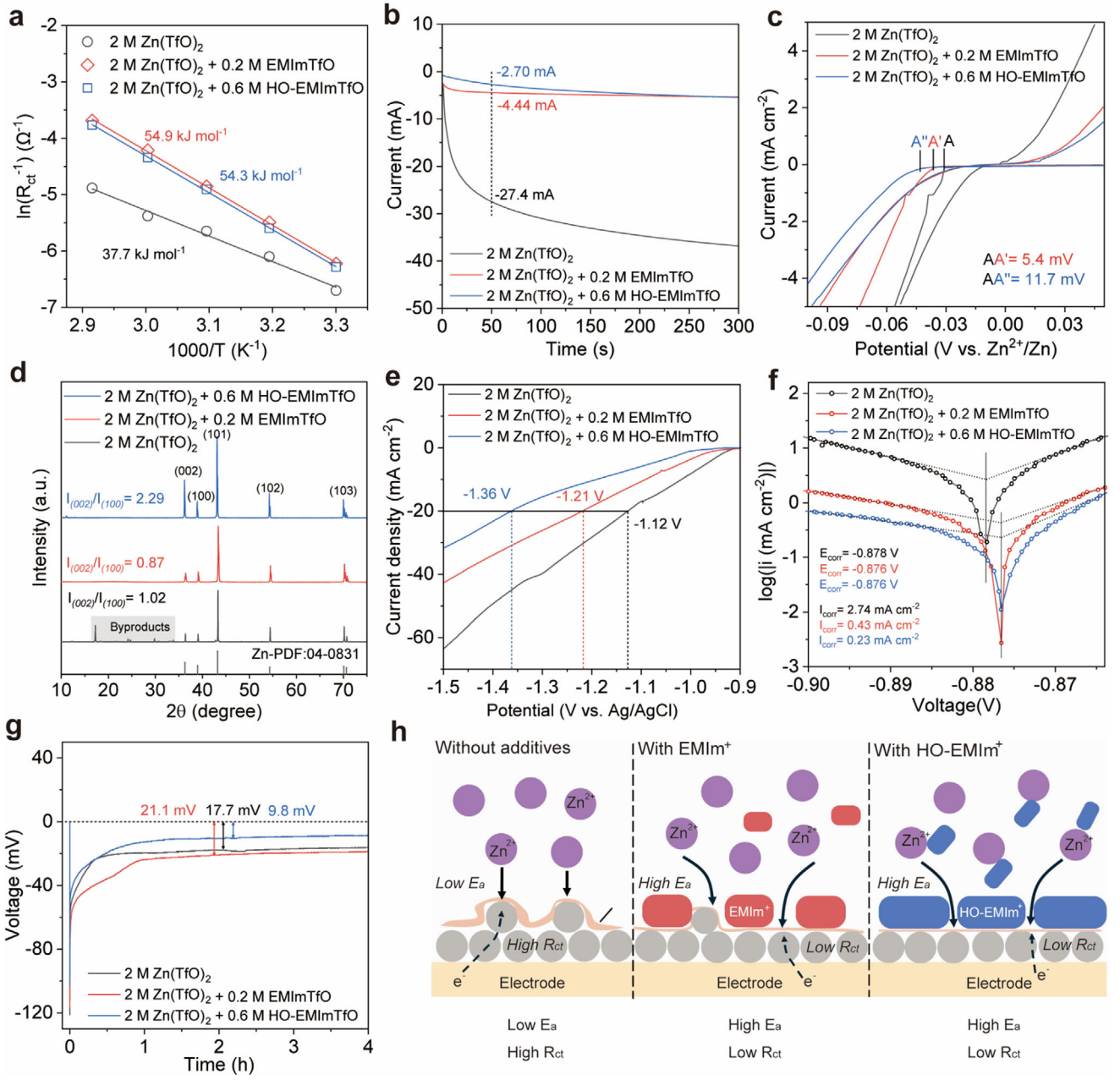

Figure 3. Zn deposition kinetics. a) Comparison of activation energies calculated using the Arrhenius equation for various electrolytes. b) Chronoamperometry curves of Zn||Zn cell with various electrolytes at -150 mV. c) CV curves of Zn||Cu cell with various electrolytes at 0.2 mV s^{-1}. d) XRD patterns of the Zn anodes with various electrolytes after 100 cycles. e) HER and f) Tafel plots of Zn electrodes in various electrolytes. g) Voltage plateau of galvanostatic Zn deposition on the Zn anode at 3 mA cm^{-2}. h) Schematic diagram of the effect of ionic liquid additives on the Zn^{2+} deposition process.

electrodeposition, we evaluated the Zn deposition potentials in different electrolytes. As shown in Figure 3g, with 0.6 M HO-EMImTfO, the Zn deposition potential was reduced to 9.8 mV, significantly lower than in the 0.2 M EMImTfO system (21.1 mV) or the 2 M $Zn(TfO)_2$ baseline (17.7 mV). This result demonstrates that the HO-EMImTfO additive effectively enhances interfacial kinetics for Zn^{2+} deposition. Overall, the results indicate that while the ionic liquid additives introduce an interfacial "ion-diversion dam" (an adsorbed cation-rich layer that increases the E_a for interfacial Zn^{2+} kinetics that includes local transport and reaction), they simultaneously lower the interfacial R_{ct} by suppressing corrosion reactions. Therefore, as depicted in Figure 3h, in the absence of additives, Zn^{2+} ions migrate directly toward the Zn electrode. This direct pathway results in a low E_a but a relatively high R_{ct} due to the formation of corrosion byproducts. In contrast, when $EMIm^+$ or $HO\text{-}EMIm^+$ is present, a cation-rich ion-diversion layer is established. This layer forces the incoming Zn^{2+} ions to diffuse laterally along the interface before

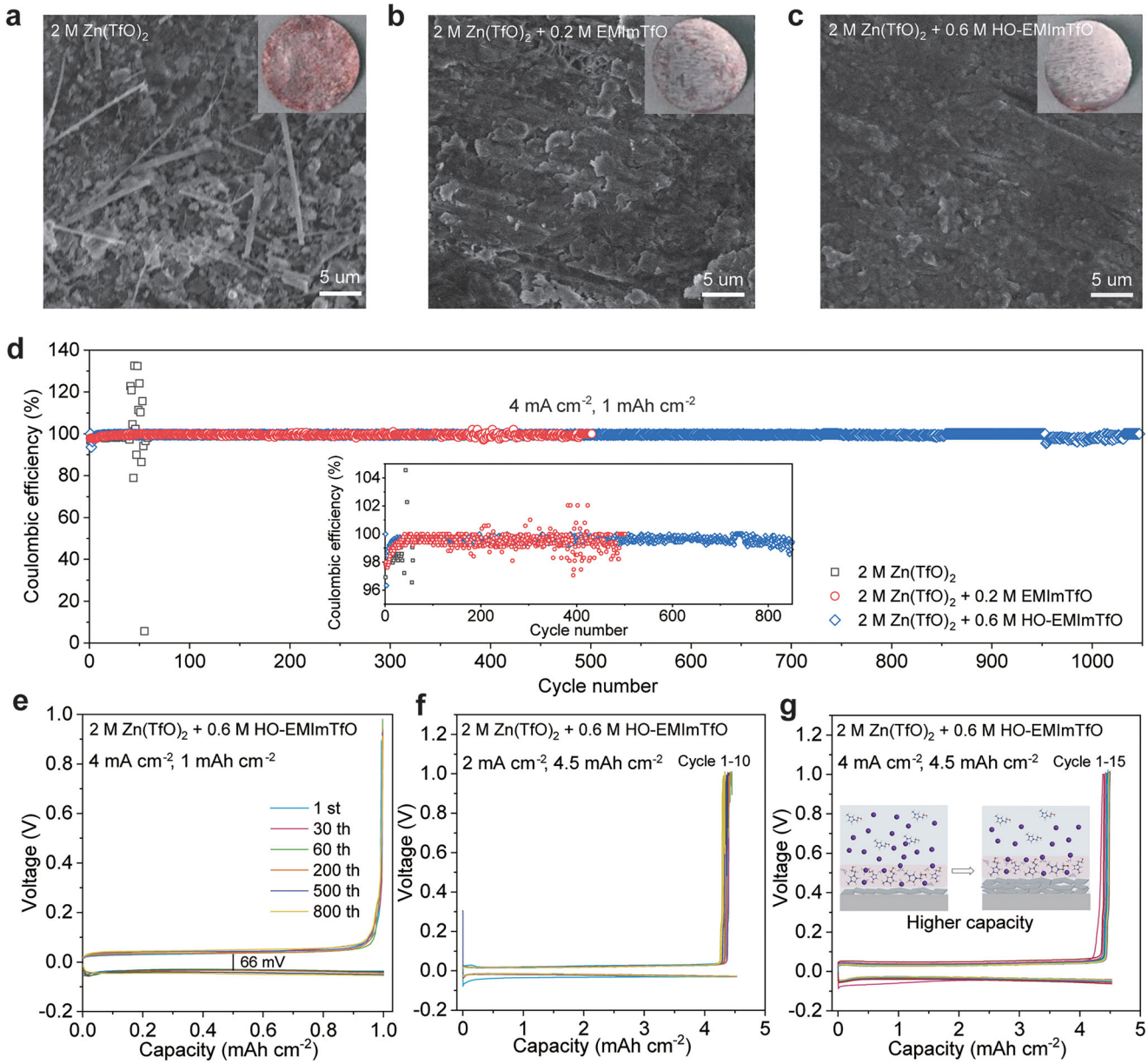

Figure 4. Zn plating/stripping reversibility. SEM images and corresponding digital photographs (insets) of Zn deposited on Cu foil using a) 2 M $Zn(TfO)_2$, b) 2 M $Zn(TfO)_2$ + 0.2 M EMImTfO, and c) 2 M $Zn(TfO)_2$ + 0.6 M HO-EMImTfO electrolytes. Current density: 4 mA cm^{-2}, areal capacity: 1 mAh cm^{-2}. d) Coulombic efficiency of Zn plating/stripping in Zn||Cu cells with different electrolytes. Voltage–capacity profiles of Zn||Cu cells using HO-EMImTfO-containing electrolytes at e) 4 mA cm^{-2}, 1 mAh cm^{-2}, f) 2 mA cm^{-2}, 4.5 mAh cm^{-2}, and g) 4 mA cm^{-2}, 4.5 mAh cm^{-2}.

reduction.[24] This "ion diversion dam" introduces a higher energetic barrier for direct perpendicular Zn^{2+} kinetics, as reflected in the increased E_a. However, its profound impact on homogenizing ion flux and drastically reducing corrosion (evidenced by lower R_{ct}) ultimately facilitates more stable and efficient Zn plating/stripping during cycling.

To assess Zn deposition morphology, SEM was performed on Zn||Cu cells containing the various electrolytes (**Figure** 4a–c). Cells incorporating HO-EMImTfO demonstrated improved and uniform Zn deposition (Figure 4c) relative to the irregular, dendritic, and pulverized deposits observed in the baseline (Figure 4a) and, to a lesser extent, the EMImTfO-containing electrolytes (Figure 4b). Cells with the HO-EMImTfO additive exhibited excellent reversibility, achieving a CE of 99.6% at lower current densities (0.5 and 1 mA cm^{-2}, Figure S22, Supporting Information). Notably, even at a high current density of 4 mA cm^{-2}, cells containing HO-EMImTfO maintained a stable average CE of 99.5% over 1000 cycles (Figure 4d). In contrast, cells with the baseline electrolyte displayed poor reversibility; the initial CE of 96.9% rapidly decayed to 86.4% within 52 cycles, leading to cell failure. The EMImTfO-containing electrolyte offered intermediate performance, showing some improvement over the baseline

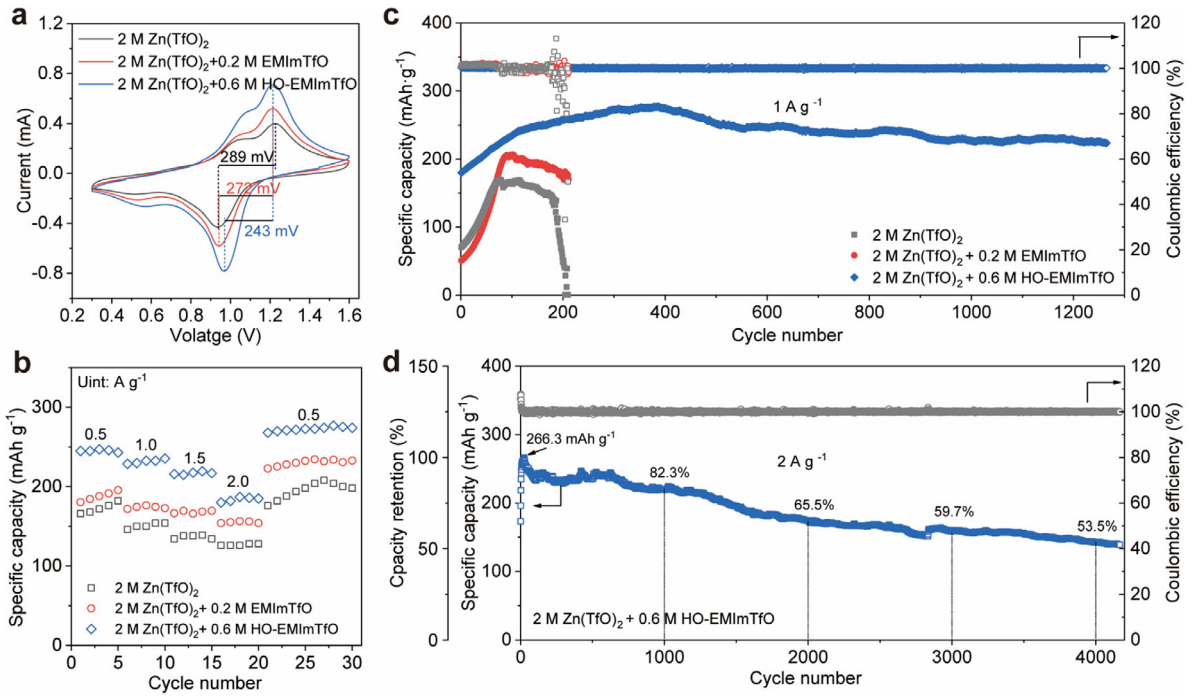

Figure 5. Full-cell performance. a) CV curves at 1 mV s^{-1} of Zn||V_2O_5 cells using various electrolytes. b) Rate capability of Zn||V_2O_5 cells using various electrolytes. c) Cycling performance of Zn||V_2O_5 cells using various electrolytes at 1 A g^{-1}. d) Cycling performance of Zn||V_2O_5 cells using HO-EMImTfO-containing electrolytes at 2 A g^{-1}. All tests were conducted at 15 °C.

but exhibiting significant CE fluctuations during extended cycling (Figure 4d, inset). Furthermore, analysis of the voltage profiles revealed that Zn||Cu cells with the HO-EMIm$^+$ additive exhibited lower overpotentials during both plating and stripping compared to cells using the baseline electrolyte (Figure 4e; Figure S23, Supporting Information).

To assess the stability imparted by the HO-EMIm$^+$-rich interfacial layer under practical conditions, Zn||Cu cells were also cycled at a high areal capacity of 4.5 mAh cm^{-2}. As shown in Figure S24 (Supporting Information), the baseline and EMImTfO-containing electrolytes exhibited large voltage fluctuations and rapidly rising overpotentials, indicating unstable Zn deposition and poor reversibility. In contrast, the HO-EMImTfO-containing electrolyte maintained stable voltage profiles at both 2 and 4 mA cm^{-2} (Figure 4f,g), with consistently high Coulombic efficiencies of 98.4% and 99.3%, respectively. These results highlight the superior interfacial stability and reversibility enabled by the HO-EMImTfO additive under high-capacity conditions, outperforming both the additive-free baseline and the EMImTfO additive. Notably, the HO-EMIm$^+$-rich layer appears to dynamically self-reconstruct during cycling to sustain its ion-regulating function, though further improvements in long-term durability are still needed. The combination of stable CE and uniform Zn deposition morphology demonstrates that the HO-EMImTfO additive significantly improves the reversibility and efficiency of Zn metal anodes, surpassing the performance of recently reported hydroxylation-free ionic liquid additives for aqueous Zn batteries (Table S1, Supporting Information).

2.4. Performance of Full Cells

Finally, to evaluate the practical viability of the HO-EMImTfO additive, Zn||V_2O_5 full cells were assembled, and their electrochemical performance was assessed. As shown in **Figure 5a**, CV profiles recorded at 1 mV s^{-1} revealed similar redox peaks for all cells, regardless of the presence or type of additive. However, the cell with the HO-EMImTfO additive exhibited a noticeably smaller voltage polarization (243 mV) compared to the system with EMImTfO (272 mV) and the baseline electrolyte (289 mV). This reduced polarization with HO-EMImTfO reflects enhanced reaction kinetics and lower internal resistance in the full cell, likely attributable to the stabilized Zn anode interface as outlined above.

Rate capability testing further demonstrated these performance improvements (Figure 5b). As current densities increased from 0.5 to 2 A g^{-1}, the Zn||V_2O_5 full cell containing 0.6 M HO-EMImTfO maintained higher capacities than the control cells. This improved rate performance is likely ascribed to the more stable Zn plating/stripping facilitated by the HO-EMImTfO additive. Furthermore, galvanostatic charge-discharge curves (Figure S25, Supporting Information) corroborated these findings, illustrating that the HO-EMImTfO additive led to lower polarization and more stable voltage plateaus across the range of current densities tested. Consequently, the HO-EMImTfO cell delivered higher discharge capacities compared to those using the baseline or EMImTfO-containing electrolytes. To gain additional insight into interfacial charge transport, impedance spectra were analyzed using the distribution of relaxation times

(DRT) method[52] (Figure S26, Supporting Information). The HO-EMImTfO electrolyte exhibited markedly lower interfacial resistance (R_{int}), charge-transfer resistance (R_{ct}), and diffusion resistance (R_{diff}), confirming its superior interfacial kinetics compared to both the baseline and EMImTfO systems.

The long-term cycling stability of the full cells further highlighted the durability enhancement provided by HO-EMImTfO. As depicted in Figure 5c, operating at a current density of 1 A g^{-1}, the Zn||V_2O_5 cell with the HO-EMImTfO additive sustained a discharge capacity of ≈223.5 mAh g^{-1} after 1265 cycles. In contrast, the cell using the baseline 2 M $Zn(TfO)_2$ electrolyte experienced rapid capacity degradation, dropping to ≈0.5 mAh g^{-1} after only 210 cycles under the same conditions. Moreover, the HO-EMImTfO-containing cell demonstrated remarkable endurance even at a high current density of 2 A g^{-1}, retaining ≈53.5% of its initial discharge capacity after 4000 cycles (Figure 5d). Even under a high current density of 5 A g^{-1}, the cell still delivered ≈173.7 mAh g^{-1} after 3500 cycles (Figure S27, Supporting Information), demonstrating outstanding rate capability and stability. The full cell maintained excellent capacity retention across a wide temperature range (Figure S28, Supporting Information), delivering ≈216.6 mAh g^{-1} at 50 °C, ≈209.5 mAh g^{-1} at 35 °C, and ≈149.2 mAh g^{-1} at 0 °C. Furthermore, using a high-mass-loading V_2O_5 cathode (25 mg cm^{-2}), the cell achieved an areal capacity of ≈6 mAh cm^{-2} at 0.1 A g^{-1} and over 2 mAh cm^{-2} at 0.2 A g^{-1} (Figure S29, Supporting Information), confirming the compatibility of the HO-EMImTfO electrolyte with high-loading electrodes. However, maintaining long-term cycling stability at such high capacities remains challenging. Therefore, further investigations are needed to understand failure mechanisms and improve interfacial stability for sustained performance.

3. Conclusion

This study demonstrates that a hydroxyl-functionalized ionic liquid, HO-EMImTfO, acts as a highly effective dual-function additive to stabilize Zn metal anodes in aqueous electrolytes. HO-EMImTfO stabilizes the Zn anode through a dual mechanism: 1) the hydroxyl-functionalized HO-$EMIm^+$ cations restructure the Zn^{2+} solvation sheath by partially replacing water molecules, thereby mitigating corrosion reactions; and 2) the cations form a surface-adsorbed ion-diversion layer that redistributes Zn^{2+} flux for uniform deposition. Electrochemical tests demonstrate that Zn||Cu cells with HO-EMImTfO additive exhibit an average Coulombic efficiency of 99.5% over 1000 cycles, while Zn||Zn symmetric cells achieve a prolonged lifespan of 1800 h. Moreover, Zn||V_2O_5 cells incorporating the HO-EMImTfO additive maintain a high capacity (≈223.5 mAh g^{-1}) over 1265 cycles, far outperforming cells without the additive. Overall, this work not only presents a highly effective additive but also validates a promising design strategy that integrates specific functionalities within ionic liquids, thereby overcoming critical challenges in aqueous Zn metal batteries and paving the way for their practical application in large-scale energy storage.

4. Experimental Section

Materials: Zn foil (100 µm thick, 99.9%) and Cu foil (30 µm, 99.9%) were obtained from Tianjin Aivisen Chemical Technology Co., Ltd. Zinc triflate ($Zn(TfO)_2$), vanadium pentoxide (V_2O_5), and 1-methyl-2-pyrrolidone (NMP) were purchased from Sigma–Aldrich. Polyvinylidene fluoride (PVDF) and Super P carbon black were obtained from Guangdong CANRD New Energy Technology Co., Ltd. 1-Ethyl-3-methylimidazolium trifluoromethanesulfonate (EMImTfO, 98%) and 1-hydroxyethyl-3-methylimidazolium trifluoromethanesulfonate (HO-EMImTfO, 97%) were purchased from Qingdao Ionike New Materials Technology Co., Ltd. Glass microfiber separators (Whatman, GF/C) were purchased from Membrane Solutions. Before use, the Zn foil was polished using sandpaper.

Electrolyte Preparation: First, $Zn(TfO)_2$ was dissolved in deionized water to create a 2 M $Zn(TfO)_2$ electrolyte solution. Next, various amounts (0.05, 0.2, 0.5, 0.8, and 1.0 M) of EMImTfO were incorporated into the 2 M $Zn(TfO)_2$ electrolyte to make the EMImTfO-containing electrolytes. Additionally, various quantities (0.2, 0.4, 0.6, 0.8, and 1.0 M) of HO-EMImTfO were also added to 2 M $Zn(TfO)_2$ to create the HO-EMImTfO-containing electrolytes.

Battery Assembly and Electrochemical Tests: CR2032-type coin cells were assembled using Zn and Cu foils, which were cut into discs with a diameter of 12 mm. In half-cell configurations, Zn and Cu foils were paired with 100 µL of electrolyte. Symmetrical cells were constructed using two Zn foils. The CE of half-cells and the cycling stability of symmetric cells were evaluated at 15 °C using a NEWARE battery testing system, simulating mildly cold conditions to assess electrolyte and interfacial stability. Electrochemical measurements, including CV, CA, Tafel corrosion analysis, LSV, and EIS, were conducted using a DH7000C electrochemical workstation. CA was performed at an overpotential of −150 mV. Tafel corrosion tests were executed in a three-electrode system, where the electrode under investigation served as the working electrode, a Pt foil acted as the counter electrode, and an Ag/AgCl (saturated KCl) electrode was used as the reference electrode. EIS measurements were carried out over a frequency range of 100 kHz to 10 mHz with an AC amplitude of 5 mV. Full cells were assembled using Zn foil as the anode and V_2O_5 as the cathode. The cathode slurry was prepared by mixing V_2O_5 (80 wt.%), Super P carbon black (10 wt.%), and PVDF binder (10 wt.%) in N-methyl-2-pyrrolidone (NMP). This slurry was then coated onto titanium foil and vacuum-dried at 60 °C for 12 h, achieving a V_2O_5 mass loading of ≈2.5 or 25 mg cm^{-2}. Finally, Zn||V_2O_5 cells were assembled using a Zn anode, the prepared V_2O_5 cathode, and 100 µL of electrolyte.

Characterization: The morphology of the samples was analyzed using a Hitachi SU8010 field emission scanning electron microscope. Elemental composition was evaluated with a Thermo Scientific Nexsa XPS system. X-ray diffraction patterns were acquired with a Bruker D8 ADVANCE diffractometer. Contact angle measurements were performed using a Krüss DSA100 instrument.

DFT Calculations: All density functional theory (DFT) calculations performed in this study were conducted using the Dmol^3 code as provided within the Materials Studio software package. Electronic exchange and correlation effects were described using the generalized gradient approximation (GGA) with the Perdew-Burke-Ernzerhof (PBE) functional, employing a double numerical plus polarization (DNP) basis set. A smearing value of 0.005 Ha was applied to the orbital occupations. The convergence criteria for energy change, maximum force, and maximum displacement were set to 1.0×10^{-5} Ha, 0.002 Ha $Å^{-1}$, and 0.005 Å, respectively. Brillouin zone integration was performed using a $3 \times 3 \times 1$ Monkhorst-Pack k-point mesh. The adsorption energy (E_{ads}) of molecules on the Zn (002) surface was defined as:

$$E_{ads} = E^*_M - E^* - E_M \quad (1)$$

where E^*_M, E^*, and E_M represent the total energy of the Zn (002) surface with the adsorbed molecule, the clean Zn (002) surface, and the isolated molecule, respectively.

To evaluate desolvation energy barriers, optimized solvation shell structures (e.g., $Zn^{2+}{\cdot}5(H_2O){\cdot}$HO-$EMIm^+$) were used to compute Gibbs free energy changes during dehydration processes. The free energy difference

(ΔG) for a representative desolvation step was calculated as:

$$\Delta G = G\left[Zn^{2+} \cdot 4\,(H_2O) \cdot HO - EMIm^{+}\right] + G\left[H_2O\right] - G\left[Zn^{2+} \cdot 5\,(H_2O) \cdot HO - EMIm^{+}\right] \quad (2)$$

The Gibbs free energy of each species was estimated by:

$$\Delta G = E_{ads}\,(H) + \Delta E_{ZPE} - T\Delta S \quad (3)$$

where ΔE_{ZPE} and ΔS were the changes in zero-point energy and entropy, respectively.

Molecular Dynamics: Molecular dynamics (MD) simulations were performed using the Forcite module as implemented within Materials Studio 2023; the COMPASS III force field was employed. Van der Waals and Coulomb interactions were handled using an atom-based method and Ewald summation, respectively, with a cutoff distance of 12.5 Å. Following an initial energy minimization step, the electrolyte systems were fully relaxed for 400 ps under NPT ensemble conditions (isothermal-isobaric: P = 1 atm, T = 298.0 K), utilizing the Nosé thermostat and Berendsen barostat under periodic boundary conditions. This relaxation period allowed the systems to achieve stability in terms of temperature, potential energy, and total energy. Once equilibrium was established, an additional 400 ps simulation was conducted under NVT ensemble conditions (canonical: constant number of particles, volume, and temperature). During this production phase, system trajectories and data were collected for subsequent radial distribution function (RDF) and coordination number (CN) calculations. The dynamic trajectories for each system were recorded at 4 ps intervals.

The CN in the first solvation sheath around Zn^{2+} was calculated as:

$$CN = 4\pi\rho \int_0^{R_M} g\,(r)\, r^2 dr \quad (4)$$

where R_M was the first local minimum after the first peak in the RDF g(r) curve, and ρ represents the atomic number density.

To further investigate interfacial behavior, MD simulations were also applied to study the density distribution and mean square displacement of Zn^{2+} in HO-EMImTfO-containing electrolyte near a Zn (002) surface. The Zn electrode was modeled as a slab consisting of four atomic layers with lateral dimensions of 38.58 Å × 38.18 Å. After geometry optimization, the electrolyte was placed above the surface, and the entire system was simulated under the NVT ensemble (T = 298.15 K) for 1000 ps with a 1 fs timestep. Trajectories were recorded every 10000 steps. Temperature was controlled via a Nosé–Hoover thermostat. Electrostatic and van der Waals interactions were treated using the same Ewald and atom-based cutoff methods as above.

Supporting Information

Supporting Information is available from the Wiley Online Library or from the author.

Acknowledgements

This work was financially supported by the Natural Science Foundation of Liaoning Province of China (No. 2022-BS-110), the Shenyang Science and Technology Talent Project Management (No. RC230828), the Basic Research Projects of Liaoning University (No. LJKLJ202435) and the Independent topic selection project of Liaoning Provincial Department of Education (No. LJ212410140011). FC thanks the University of Bayreuth and the Bavarian Center for Battery Technology (BayBatt) for providing start-up funds, the Deutsche Forschungsgemeinschaft (DFG, German Research Foundation) (No.533115776), and the Support from the BayBatt Cell Technology Center is gratefully acknowledged as funded by the Deutsche Forschungsgemeinschaft (DFG, German Research Foundation) (No. INST 91/452-1).

Conflict of Interest

The authors declare no conflict of interest.

Data Availability Statement

The data supporting the findings of this study are available in this article and its Supporting Information. Additional data may be available from the corresponding author upon reasonable request.

Keywords

aqueous batteries, electrolyte additives, ionic liquids, Zn anodes

Received: May 20, 2025
Revised: July 4, 2025
Published online: July 25, 2025

[1] N. Zhang, X. Chen, M. Yu, Z. Niu, F. Cheng, J. Chen, *Chem. Soc. Rev.* **2020**, *49*, 4203.
[2] J. Zhu, Z. Tie, S. Bi, Z. Niu, *Angew. Chem., Int. Ed.* **2024**, *63*, 202403712.
[3] J. H. Park, C. Choi, J. B. Park, S. Yu, D. W. Kim, *Adv. Energy Mater.* **2023**, *14*, 2302493.
[4] H. Yan, S. Li, J. Zhong, B. Li, *Nano-Micro Lett.* **2023**, *16*, 15.
[5] T. Zhou, R. Huang, Q. Lu, P. Liu, L. Hu, K. Zhang, P. Bai, R. Xu, X. Cao, Z. Sun, S. Duan, R. Liu, Y. Qin, X. Sun, Y. Zhang, Y. Li, Y. Yan, M. Liu, X. Wang, *Energy Storage Mater.* **2024**, *72*, 103689.
[6] Z. Guo, L. Fan, C. Zhao, A. Chen, N. Liu, Y. Zhang, N. Zhang, *Adv. Mater.* **2022**, *34*, 2105133.
[7] K. Zhao, C. Wang, Y. Yu, M. Yan, Q. Wei, P. He, Y. Dong, Z. Zhang, X. Wang, L. Mai, *Adv. Mater. Interaces* **2018**, *5*, 1800848.
[8] Y. Liang, D. Ma, N. Zhao, Y. Wang, M. Yang, J. Ruan, G. Yang, H. Mi, C. He, P. Zhang, *Adv. Funct. Mater.* **2022**, *32*, 212936.
[9] Y. Zong, H. He, Y. Wang, M. Wu, X. Ren, Z. Bai, N. Wang, X. Ning, S. X. Dou, *Adv. Energy Mater.* **2023**, *13*, 2300403.
[10] M. Xu, J. Chen, Y. Zhang, B. Raza, C. Lai, J. Wang, *J. Energy Chem.* **2022**, *73*, 575.
[11] B. Zhang, J. Yao, C. Wu, Y. Li, J. Liu, J. Wang, T. Xiao, T. Zhang, D. Cai, J. Wu, Z. W. Seh, S. Xi, H. Wang, W. Sun, H. Wan, H. J. Fan, *Nat. Commun.* **2025**, *16*, 71.
[12] H. Li, S. Li, R. Hou, Y. Rao, S. Guo, Z. Chang, H. Zhou, *Chem. Soc. Rev.* **2024**, *53*, 7742.
[13] Z. Liang, C. Li, D. Zuo, L. Zeng, T. Ling, J. Han, J. Wan, *Energy Storage Mater.* **2023**, *63*, 102980.
[14] Z. Li, A. W. Robertson, *Batter. Energy* **2022**, *2*, 20220029.
[15] J. Cao, F. Zhao, W. Guan, X. Yang, Q. Zhao, L. Gao, X. Ren, G. Wu, A. Liu, *Small* **2024**, *20*, 2400221.
[16] J. N. Hao, L. B. Yuan, C. Ye, D. L. Chao, K. Davey, Z. P. Guo, S. Z. Qiao, *Angew. Chem., Int. Ed.* **2021**, *60*, 7366.
[17] L. Ma, J. Vatamanu, N. T. Hahn, T. P. Pollard, O. Borodin, V. Petkov, M. A. Schroeder, Y. Ren, M. S. Ding, C. Luo, J. L. Allen, C. Wang, K. Xu, *Proc. Natl. Acad. Sci. U.S.A.* **2022**, *119*, 2121138119.
[18] N. Wang, Y. Yang, X. Qiu, X. Dong, Y. Wang, Y. Xia, *ChemSusChem* **2020**, *13*, 5556.
[19] X. Li, H. Wang, X. Sun, J. Li, Y.-N. Liu, *ACS Appl. Energy Mater.* **2021**, *4*, 12718.
[20] F. Bu, Y. Gao, W. Zhao, Q. Cao, Y. Deng, J. Chen, J. Pu, J. Yang, Y. Wang, N. Yang, T. Meng, X. Liu, C. Guan, *Angew. Chem. Int. Ed* **2024**, *63*, 202318496.
[21] Q. Hu, J. Hu, L. Li, Q. Ran, Y. Ji, X. Liu, J. Zhao, B. Xu, *Energy Storage Mater.* **2023**, *54*, 374.

[22] T. Liu, X. Dong, B. Tang, R. Zhao, J. Xu, H. Li, S. Gao, Y. Fang, D. Chao, Z. Zhou, *J. Energy Chem.* **2024**, *98*, 311.
[23] H. Wang, W. Ye, B. Yin, K. Wang, M. S. Riaz, B. B. Xie, Y. Zhong, Y. Hu, *Angew. Chem., Int. Ed.* **2023**, *62*, 20221887.
[24] X. Liao, S. Chen, J. Chen, Y. Li, W. Wang, T. Lu, Z. Chen, L. Cao, Y. Wang, R. Huang, X. Sun, R. Lv, H. Wang, *Proc. Natl. Acad. Sci. U.S.A.* **2024**, *121*, 2317796121.
[25] N. Chernov, D. Dolgopyat, *Phys. Rev. Lett.* **2007**, *99*, 030601.
[26] H. J. Guo, X. J. Chen, R. Shu, X. B. Zhong, L. X. Zhang, Y. X. Song, *J. Colloid Interface Sci.* **2025**, *678*, 627.
[27] J. Ke, Z. Wen, Y. Yang, R. Tang, Y. Tang, M. Ye, X. Liu, Y. Zhang, C. C. Li, *Adv. Funct. Mater.* **2023**, *33*, 2301129.
[28] Y. Lv, Y. Xiao, S. Xu, F. Huo, Y. Chen, M. Zhao, L. Liu, C. Su, Y. Zhu, S. Chen, *J. Mater. Chem. A* **2022**, *10*, 16952.
[29] Y. X. Song, J. Wang, X. B. Zhong, Y. H. Zhang, K. Wang, X. H. Guo, H. J. Guo, G. P. Lei, H. T. Liu, G. K. Wang, P. G. Ji, X. Zhang, U. Khalilov, J. F. Liang, R. Wen, *J. Colloid Interface Sci.* **2024**, *665*, 711.
[30] L. Yu, J. Huang, S. Wang, L. Qi, S. Wang, C. Chen, *Adv. Mater.* **2023**, *35*, 2210789.
[31] M. Zhao, J. Rong, F. Huo, Y. Lv, B. Yue, Y. Xiao, Y. Chen, G. Hou, J. Qiu, S. Chen, *Adv. Mater.* **2022**, *34*, 2203153.
[32] Z. Zhao, J. Lai, D. T. Ho, Y. Lei, J. Yin, L. Chen, U. Schwingenschlögl, H. N. Alshareef, *ACS Energy Lett.* **2023**, *8*, 608.
[33] X. Wu, Y. Dai, N. W. Li, X. C. Chen, L. Yu, *eScience* **2024**, *4*, 100173.
[34] X. Wang, L. Liu, Z. Hu, C. Han, X. Xu, S. Dou, W. Li, *Chem. Sci.* **2024**, *15*, 17348.
[35] S. Chen, D. Ji, Q. Chen, J. Ma, S. Hou, J. Zhang, *Nat. Commun.* **2023**, *14*, 3526.
[36] G. Li, Z. Zhao, S. Zhang, J. Zhao, M. Li, J. Xie, C. Xia, Z. Guo, *Nat. Commun.* **2023**, *14*, 6526.
[37] J. Feng, X. Li, Y. Ouyang, H. Zhao, N. Li, K. Xi, J. Liang, S. Ding, *Angew. Chem., Int. Ed.* **2024**, *63*, 202407194.
[38] R. Han, T. Jiang, Z. Wang, R. Xue, X. Liu, Y. Tang, Z. Qi, Y. Ma, *Adv. Funct. Mater.* **2024**, *35*, 2412255.
[39] Q. Zhang, K. Xia, Y. Ma, Y. Lu, Y. Li, Q. Wang, X. Yang, H. Huang, *ACS Energy Lett.* **2021**, *6*, 2704.
[40] Z. Zhang, B. Xi, X. Ma, W. Chen, J. Feng, S. Xiong, *SusMat* **2022**, *2*, 114.
[41] S.-J. Zhang, J. Hao, D. Luo, P.-F. Zhang, B. Zhang, K. Davey, Z. Lin, S.-Z. Qiao, *Adv. Energy Mater.* **2021**, *11*, 2102010.
[42] Y. Zhang, X. Li, Z. Wang, H. Liu, J. Chen, Y. Zhao, J. Huang, X. Wang, *Adv. Funct. Mater.* **2023**, *33*, 2304567.
[43] R. Wang, M. Yao, M. Yang, J. Zhu, J. Chen, Z. Niu, *Proc. Natl. Acad. Sci. U.S.A.* **2023**, *120*, 2221980120.
[44] X. Yu, Z. Li, X. Wu, H. Zhang, Q. Zhao, H. Liang, H. Wang, D. Chao, F. Wang, Y. Qiao, H. Zhou, S.-G. Sun, *Joule* **2023**, *7*, 1145.
[45] Z. Zhao, J. Zhao, Z. Hu, J. Li, J. Li, Y. Zhang, C. Wang, G. Cui, *Energy Environ. Sci.* **2019**, *12*, 1938.
[46] H. T. Lu, X. L. Zhang, M. H. Luo, K. S. Cao, Y. H. Lu, B. B. Xu, H. G. Pan, K. Tao, Y. Z. Jiang, *Adv. Funct. Mater.* **2021**, *31*, 2103514.
[47] W. Yuan, X. Nie, Y. Wang, X. Li, G. Ma, Y. Wang, S. Shen, N. Zhang, *ACS Nano* **2023**, *17*, 23861.
[48] H. Zhang, Y. Zhong, J. Li, Y. Liao, J. Zeng, Y. Shen, L. Yuan, Z. Li, Y. Huan, *Adv. Energy Mater.* **2023**, *13*, 2203254.
[49] Z. Zhang, Y. Zhang, M. Ye, Z. Wen, Y. Tang, X. Liu, C. C. Li, *Angew. Chem., Int. Ed.* **2023**, *62*, 202311032.
[50] J. Zhang, P. Li, Y. Wang, Z. Zhao, Z. Peng, *Adv. Funct. Mater.* **2023**, *33*, 2305804.
[51] Y. Song, M. Chen, Z. Zhong, Z. Liu, S. Liang, G. Fang, *Nat. Commun.* **2025**, *16*, 3142.
[52] T. H. Wan, M. Saccoccio, C. Chen, F. Ciucci, *Electrochim. Acta* **2015**, *184*, 483.